Pergamon

Int. J. Solids Structures Vol. 33, No. 12, pp. 1757–1779, 1996

0020-7683/96 $15.00 + .00

0020-7683(95)00123-9

A FINITE ELEMENT METHOD FOR ELECTROSTRICTIVE CERAMIC DEVICES

CRAIG L. HOM and NATARAJAN SHANKAR
Martin Marietta Laboratories, Lockheed Martin Corporation, 1450 South Rolling Road, Baltimore, MD 21227-3898, U.S.A.

(*Received* 9 *September* 1994; *in revised form* 17 *May* 1995)

Abstract—A nonlinear, static finite element technique is developed and implemented for electrostrictive ceramic solids. This numerical method is based on Toupin's elastic dielectric theory and models full electromechanical coupling in the solid via the Maxwell stress and constitutive equations [Toupin, R. A. (1956). The elastic dielectric. *J. Rational Mech. Anal.* **5**, 849–915; Toupin, R. A. (1963). A dynamical theory of elastic dielectrics. *Int. J. Engng Sci.* **1**, 101–126]. The formulation incorporates the constitutive model of Hom and Shankar [(1994). A fully coupled constitutive model for electrostrictive ceramic materials. *J. Intell. Mater. Syst. Struct.* **5**, 795–801]. This model simulates polarization saturation at high electric fields and nonlinear coupling of the mechanical and electric field variables. The finite element technique is demonstrated by solving the problem of a multilayered actuator constructed from a lead-magnesium-niobate electrostrictor. Both the electric field and stress state are computed near the tip of an internal electrode. The results show that the nonlinear dielectric behavior significantly alters the electric field near the tip to form a stress singularity. An analytical solution of the internal electrode problem is presented and compared with the finite element predictions for verification. The comparison shows a good qualitative agreement between the two solutions. Finally, the numerical results are used to examine crack nucleation and growth from the electrode tip.

1. INTRODUCTION

In the last ten years, considerable research has been devoted to incorporating piezoelectric and electrostrictive ceramic devices into structural systems as either sensors that detect mechanical forces or as actuators that create mechanical motion. Recent interest has focused on "smart" structures, in which a feedback loop ties the sensors and actuators together. In this sense the system is "smart" since it is able to recognize and respond to the surrounding environment. Some potential uses for smart structures include vibration isolation or cancellation, noise control, and dynamic tailoring of airfoils [Gandhi and Thompson (1992)]. In addition to smart systems, electromechanical ceramics have found non-structural commercial use as precision positioners for electro-optical applications, medical imaging transducers, dot-matrix printer heads, and electromechanical switches [Uchino (1986)].

Both piezoelectrics and electrostrictors are ferroelectric: they exhibit a spontaneous electric polarization below a transition temperature called the Curie temperature. Piezoelectrics are usually poled to align the polarization in a specific direction, and they have near-linear electromechanical coupling. In contrast, electrostrictors are usually unpoled, and they have nonlinear electromechanical coupling. Electrostrictors have a symmetric crystal structure, so reversing the direction of electric polarization does not change the induced strain. While all dielectrics display electrostrictive behavior, the typical induced strains are often small. However, a special class of ferroelectrics, called relaxor ferroelectrics, can sustain very large polarizations, which induce significant electrostrictive strain, approximately 0.1% for $Pb(Mg_{1/3}Nb_{2/3})O_3$ (PMN). The spontaneous polarization in these materials is not lost suddenly at a specific Curie temperature, but decays slowly with increasing temperature. Somolenski *et al.* (1961) and Cross (1987) have postulated that a random ordering of ions in relaxor ferroelectrics creates a microscopic mixture of polar and nonpolar regions that becomes more polar with decreasing temperature. The dielectric hysteresis disappears in this diffuse transition region before the spontaneous polarization, so mechanical actuation is possible with less hysteresis than conventional piezoelectrics.

Electrostriction has been experimentally investigated in PMN [Kuwata, Uchino and Nomura (1980); Uchino *et al.* (1980)], PMN-$PbTiO_3$ [Pilgrim *et al.* (1992)]; $BaTiO_3$ [Abe *et al.* (1986)]; and Pb(La, Zr, Ti)O_3 [Kirkby (1981)]. Recently, Hom and Shankar (1994) developed a nonlinear, electromechanical constitutive model for relaxor ferroelectrics. Following a phenomenological approach, this model is based on the assumptions that electrostrictive strain is proportional to the square of polarization and that the polarization saturates at high fields.

Because of the complicated behavior of relaxor ferroelectrics, devices constructed from these materials require numerical or analytical simulation to optimize both performance and reliability. The popular finite element method is a potential design tool for achieving these goals. Finite element models of the stand-alone device or the device embedded in a structure could predict both displacement and load response. In addition, analyses of stress concentrations and defects using finite element techniques could suggest design modifications that improve the device's reliability [Taylor *et al.* (1988); Winzer *et al.* (1989); and Yang and Suo (1994)].

While linear finite element methods for piezoelectric materials are relatively mature [Allik and Hughes (1970), Kawaga and Yamabuchi (1974); Allik *et al.* (1974)], numerical formulations for modeling electrostrictive behavior are just beginning to emerge. Recently, Winzer *et al.* (1989) approximated electrostrictive behavior in multilayered actuators with finite element analysis. They assumed a static electric field distribution in the device, and computed the corresponding stress-free electrostrictive strain. The resulting values were used as a residual strain in a linear, static structural finite element code. However, their analysis did not couple the ceramic's dielectric behavior with the stress field.

In this paper, we present a nonlinear, static finite element method for analyzing the performance and reliability of electrostrictive ceramic devices. We based our numerical formulation on Toupin's (1956, 1963) electromechanical theory for an elastic dielectric and Hom and Shankar's constitutive law for a relaxor ferroelectric. Thus our approach accounts for full coupling between the electric and mechanical field variables. We demonstrate our finite element formulation by analyzing a multilayered electrostrictive actuator similar to the configuration described by Winzer *et al.* (1989) and studied analytically by Yang and Suo (1994). We also present a new analytical solution for the multilayered internal electrode problem to compare with the finite element computations. Finally, the numerical results are used to study internal cracking in the device.

2. GOVERNING EQUATIONS FOR STATIC ELECTROMECHANICS

In this section, we present the field equations and boundary conditions for a deformable solid containing electric charge and subject to mechanical forces. These equations ensure that both Maxwell-Lorentz's theory of electrostatics and mechanical static equilibrium are satisfied. Our formulation follows the work of Toupin (1956, 1963) and Eringen (1963), and forms the basis of our finite element method. However, unlike Toupin and Eringen, we limit our formulation to small deformations and rotations.

Consider the continuous, solid body occupying region V in space and enclosed by surface ∂V shown in Fig. 1. Let V_∞ denote the remainder of space, which for simplicity, we assume is a vacuum containing no electric charge. The position of any point in the body and the surrounding vacuum is defined by the vector $\mathbf{x}$. The solid is composed of both conducting material in which the electric charge is free to move and dielectric material in which the electric charge is fixed in place. The interfaces between the dielectrics and conductors are defined by the surfaces Σ, and are assumed to be perfect bonds. The vector $\mathbf{n}$ denotes the normal of surfaces ∂V and Σ. For ∂V, $\mathbf{n}$ is directed outward from the solid.

Electrostatics

If the body has an extrinsic volume electric-charge density of q in V and an extrinsic surface electric-charge density of ω on ∂V and Σ, then the total extrinsic charge, Q, on the body is given by

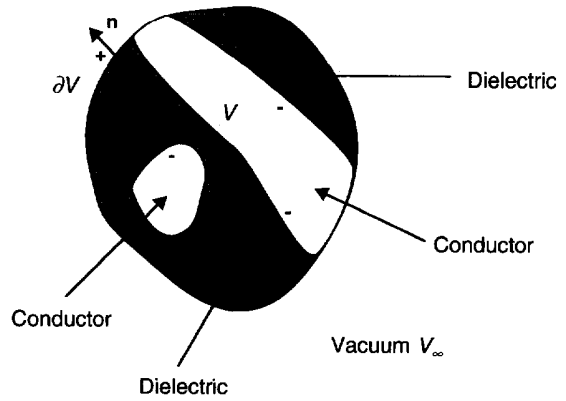

Fig. 1. An electrodeformable body composed of conductors and dielectrics, and surrounded by a vaccum V_∞

$$Q = \int_V q \, dV + \int_{\partial V + \Sigma} \omega \, dS. \tag{1}$$

If a small test charge, Q_o, is introduced in the neighborhood of the solid body, an electric force resulting from Q acts upon it. The electric field **E** is a vector defined so that the force vector **F** on the test charge is given by:

$$\mathbf{F} = Q_o \mathbf{E}. \tag{2}$$

The Maxwell-Lorentz theory governs the behavior of the electric field. For static conditions, in which all electric charges are stationary, an electric potential ϕ exists such that

$$\mathbf{E} = -\frac{\partial \phi}{\partial x}. \tag{3}$$

E may be discontinuous across the surfaces ∂V and Σ; however, the component of **E** tangent to those surfaces must be continuous. Consequently,

$$[\![\mathbf{E}]\!] \times \mathbf{n} = 0. \tag{4}$$

In this paper, $[\![\mathbf{A}]\!]$ denotes the jump of **A** across a surface from interior ($\mathbf{A}^-$) to exterior ($\mathbf{A}^+$) as defined by **n**, i.e. $[\![\mathbf{A}]\!] = \mathbf{A}^+ - \mathbf{A}^-$.

The presence of an electric field means that electric forces are exerted on any charged particle in the solid. In the conductors, extrinsic charge is distributed along the surface, and the electric field in the material's interior is zero. In the dielectrics, the electric field polarizes the material by inducing dipole moments. The polarization vector **P** of a dielectric is quantitatively defined as the density of the induced dipoles; like **E**, it can be discontinuous across surface boundaries. Polarization of the solid's dielectrics creates an induced volume charge density of $-(\partial/\partial \mathbf{x}) \cdot \mathbf{P}$ that is bound in V, and an induced surface charge of $-\mathbf{n} \cdot [\![\mathbf{P}]\!]$ that is bound on ∂V and Σ [Böttcher (1952)]. In this paper we refer to the sum of the induced and extrinsic charges as the effective charge. For the vacuum V_∞ and the solid's conductors, **P** equals zero and consequently no additional charge is induced.

Gauss's law for electrostatics states that the net outward electric flux through any closed surface is equal to the total enclosed charge, both induced and extrinsic, divided by the permittivity of free space, κ_o. If the closed surface is ∂V, then this statement can be expressed for the solid body as

$$\int_{\partial V} \mathbf{n}\cdot\mathbf{E}^{+}\,\mathrm{d}S = \frac{1}{\kappa_o}\left(\int_V \left[q-\left(\frac{\partial}{\partial \mathbf{x}}\right)\cdot\mathbf{P}\right]\mathrm{d}V+\int_{\partial V+\Sigma}[\omega-\mathbf{n}\cdot[\![\mathbf{P}]\!]]\,\mathrm{d}S\right). \tag{5}$$

Applying the generalized Green-Gauss theorem (Appendix A) to the electric field, eqn (5) can be rewritten as

$$\kappa_o\int_V\left(\frac{\partial}{\partial \mathbf{x}}\right)\cdot\mathbf{E}\,\mathrm{d}V+\kappa_o\int_{\partial V+\Sigma}\mathbf{n}\cdot[\![\mathbf{E}]\!]\,\mathrm{d}S=\int_V\left[q-\left(\frac{\partial}{\partial \mathbf{x}}\right)\cdot\mathbf{P}\right]\mathrm{d}V+\int_{\partial V+\Sigma}[\omega-\mathbf{n}\cdot[\![\mathbf{P}]\!]]\,\mathrm{d}S. \tag{6}$$

Since this relation must hold for arbitrary V, ∂V, and Σ, Gauss's law for the dielectric/conductor solid becomes

$$\kappa_o\left(\frac{\partial}{\partial \mathbf{x}}\right)\cdot\mathbf{E}=q-\left(\frac{\partial}{\partial \mathbf{x}}\right)\cdot\mathbf{P}\quad\text{in } V,\quad\text{and} \tag{7}$$

$$\kappa_o\mathbf{n}\cdot[\![\mathbf{E}]\!]=\omega-\mathbf{n}\cdot[\![\mathbf{P}]\!]\quad\text{on } \partial V \text{ and } \Sigma. \tag{8}$$

The same calculation can be performed for the vacuum surrounding the solid by assuming that it and the solid are completely enclosed by a fictitious surface ∂V_∞. Since the charge density in V_∞ is zero, Gauss's law yields

$$\int_{\partial V_\infty}\mathbf{n}\cdot\mathbf{E}^{+}\,\mathrm{d}S-\int_{\partial V}\mathbf{n}\cdot\mathbf{E}^{+}\,\mathrm{d}S=0, \tag{9}$$

where $\mathbf{n}$ and $\mathbf{E}^{+}$ on ∂V are the exterior normal and exterior electric field relative to the solid. The vacuum does not contain any discontinuities in $\mathbf{E}$, therefore we can apply the divergence theorem to (9) to obtain

$$\left(\frac{\partial}{\partial \mathbf{x}}\right)\cdot\mathbf{E}=0\text{ in } V_\infty. \tag{10}$$

Mechanical equilibrium

In addition to applied mechanical forces, an electric body force and electric surface tractions act on the solid as a result of the presence of the induced and extrinsic charges. The Lorentz body force caused by the distributed volume charges in V is $[q-(\partial/\partial\mathbf{x})\cdot\mathbf{P}]\mathbf{E}$, which follows directly from eqn (2). The electric surface traction, $\mathbf{T}^E$, on ∂V and Σ is given by Toupin (1963) as

$$\mathbf{T}^E=(\omega-\mathbf{n}\cdot[\![\mathbf{P}]\!])\left(\mathbf{E}^{+}-\frac{[\![\mathbf{E}]\!]}{2}\right). \tag{11}$$

Considering these additional electric forces, mechanical equilibrium for the body can be written as

$$\int_V\mathbf{f}\,\mathrm{d}V+\int_{\partial V}\mathbf{T}\,\mathrm{d}S+\int_V\left[q-\left(\frac{\partial}{\partial \mathbf{x}}\right)\cdot\mathbf{P}\right]\mathbf{E}\,\mathrm{d}V+\int_{\partial V+\Sigma}(\omega-\mathbf{n}\cdot[\![\mathbf{P}]\!])\left(\mathbf{E}^{+}-\frac{[\![\mathbf{E}]\!]}{2}\right)\mathrm{d}S=0, \tag{12}$$

where $\mathbf{f}$ is the mechanical body force in V and $\mathbf{T}$ is the mechanical surface traction on ∂V.

Now we define the stress tensor $\boldsymbol{\sigma}$ such that

$$-\mathbf{n}\cdot[\![\boldsymbol{\sigma}]\!] = \mathbf{T}+\mathbf{n}\cdot[\![\mathbf{m}]\!] \tag{13}$$

on ∂V and Σ, where $\mathbf{T}$ equals zero on Σ. $\mathbf{m}$ is the Maxwell electrostatic stress tensor, which Toupin (1963) and Eringen (1963) have defined as

$$\mathbf{m} = \kappa_o\left(\mathbf{E}\,\mathbf{E}-\frac{\mathbf{E}\cdot\mathbf{E}}{2}\mathbf{I}\right). \tag{14}$$

$\mathbf{E}\,\mathbf{E}$ denotes the diatic product of $\mathbf{E}$ with itself, and $\mathbf{I}$ is the identity matrix. Toupin (1963) has shown that the definition of Maxwell stress given by eqn (14) and the conservation of angular moment leads to a symmetric stress tensor $\boldsymbol{\sigma}$.

Using eqns (3), (7), and (14), we show that the divergence of Maxwell stress is equal to the Lorentz force,

$$\left(\frac{\partial}{\partial\mathbf{x}}\right)\cdot\mathbf{m} = \left(\mathrm{q}-\left(\frac{\partial}{\partial\mathbf{x}}\right)\cdot\mathbf{P}\right)\mathbf{E} \quad \text{in } V. \tag{15}$$

Also we combine eqns (4), (8) and (14) to obtain the jump condition for the Maxwell stress,

$$\mathbf{n}\cdot[\![\mathbf{m}]\!] = (\omega-\mathbf{n}\cdot[\![\mathbf{P}]\!])\left(\mathbf{E}^+-\frac{[\![\mathbf{E}]\!]}{2}\right) \quad \text{on } \partial V \text{ and } \Sigma. \tag{16}$$

Therefore the components of Maxwell stress normal to the surface equal the electric force. Using (15), (16) and the generalized Green-Gauss theorem, eqn (12) can be converted to

$$\int_V\left[\left(\frac{\partial}{\partial\mathbf{x}}\right)\cdot(\boldsymbol{\sigma}+\mathbf{m})+\mathbf{f}\right]\mathrm{d}V-\int_{\partial V}\mathbf{n}\cdot\boldsymbol{\sigma}^+\,\mathrm{d}S = 0. \tag{17}$$

Since this relation must be true for arbitrary V and ∂V, the two integrands must be zero, and the mechanical equilibrium for the solid reduces to

$$\left(\frac{\partial}{\partial\mathbf{x}}\right)\cdot(\boldsymbol{\sigma}+\mathbf{m})+\mathbf{f} = 0 \text{ in } V \quad \text{and} \tag{18}$$

$$\mathbf{n}\cdot\boldsymbol{\sigma}^+ = 0 \quad \text{on } \partial V. \tag{19}$$

Constitutive behavior

Finally, we need constitutive relations for the dielectric and conducting materials in the solid. Toupin (1963) has shown that conservation of energy for an element of the solid leads to

$$\mathrm{d}U = \boldsymbol{\sigma}:\mathrm{d}\boldsymbol{\varepsilon}+\mathbf{E}\cdot\mathrm{d}\mathbf{P} \tag{20}$$

where U is the internal energy density of the solid and $\boldsymbol{\varepsilon}$ is the strain tensor. For small deflections and rotations, we define the strain measure as

$$\boldsymbol{\varepsilon} = \frac{1}{2}\left(\frac{\partial\mathbf{u}}{\partial\mathbf{x}}+\left[\frac{\partial\mathbf{u}}{\partial\mathbf{x}}\right]^T\right) \tag{21}$$

where the vector $\mathbf{u}$ is the displacement of a point in the solid from its initial position, and

the superscript T denotes the transpose of a tensor. Equation (20) indicates that U depends only on the internal state variables, $\boldsymbol{\varepsilon}$ and $\mathbf{P}$. Using eqn (20) and the chain rule on U, we obtain

$$\boldsymbol{\sigma} = \frac{\partial U}{\partial \boldsymbol{\varepsilon}} \tag{22}$$

and

$$\mathbf{E} = \frac{\partial U}{\partial \mathbf{P}}, \tag{23}$$

which relate the internal state variables, $\boldsymbol{\varepsilon}$ and $\mathbf{P}$, to the state functions, $\boldsymbol{\sigma}$ and $\mathbf{E}$. In a later section, we present an explicit set of constitutive laws for relaxor ferroelectrics.

Summary of equations

From the governing equation presented in this section, we see that the electrical variables, $\mathbf{E}$ and $\mathbf{P}$, are coupled to the mechanical variables, $\boldsymbol{\sigma}$ and $\boldsymbol{\varepsilon}$, at two levels. First, the electric fields directly generate distributed forces via the Maxwell stress, which in turn affect the mechanical equilibrium of the solid. The resulting stresses depend on the second-order terms of electric field. This nonlinear phenomena is traditionally called electrostriction and occurs in both dielectrics and conductors [Landau and Lifshitz (1960)]. The resulting electrostrictive stresses are typically small (10^{-5} MPa for a 1MV/m field) except at field singularities, such as electrode or conducting crack tips [McMeeking (1987, 1989)]. This form of electrostriction has no converse effect, since the mechanical stress state does not directly influence the electrostatic balance.

The second level of coupling occurs in the constitutive behavior of the dielectric material, expressed by eqns (22) and (23). Full coupling takes place because polarization induces strain, while mechanical stress changes the polarization. Piezoelectricity is the most common example of a fully coupled electromechanical material. The coupling is approximately linear, and Voight's (1910) linear constitutive law is typically used to model piezoelectric behavior. In electrostrictive materials, such as relaxor ferroelectrics, the coupling has a nonlinear dependence on polarization. Our formulation accounts for both types of electrostriction: electric body force and constitutive response.

3. FINITE ELEMENT FORMULATION

A Galerkin-weighted residual finite element method [Zienkiewicz and Taylor (1989)] was developed for the electromechanical field problem presented in the previous section. This method uses a modified Newton procedure to solve the resulting nonlinear finite element equations for the field variables, $\mathbf{u}$ and ϕ.

If the governing equations in regions V and V_∞ and the boundary conditions on ∂V and Σ hold, then a weak statement of the problem is

$$\begin{aligned}\int_V \left[\left(\frac{\partial}{\partial \mathbf{x}}\right)\cdot(\boldsymbol{\sigma}+\mathbf{m})+\mathbf{f}\right]\cdot\mathbf{W}_u\,\mathrm{d}V+\int_V\left[\left(\frac{\partial}{\partial \mathbf{x}}\right)\cdot(\kappa_o\mathbf{E}+\mathbf{P})-q\right]W_\phi\,\mathrm{d}V\\ +\int_{V_\infty}\kappa_o\left[\left(\frac{\partial}{\partial \mathbf{x}}\right)\cdot\mathbf{E}\right]W_\phi\,\mathrm{d}V+\int_{\partial V+\Sigma}[\mathbf{n}\cdot[\![\boldsymbol{\sigma}+\mathbf{m}]\!]+\mathbf{T}]\cdot\mathbf{W}_u\,\mathrm{d}S-\int_{\partial V}\mathbf{n}\cdot\boldsymbol{\sigma}^+\cdot\mathbf{W}_u\,\mathrm{d}S\\ +\int_{\partial V+\Sigma}[\mathbf{n}\cdot[\![\kappa_o\mathbf{E}+\mathbf{P}]\!]-\omega]W_\phi\,\mathrm{d}S=0\end{aligned} \tag{24}$$

where $\mathbf{W}_u$ and W_ϕ are arbitrary weight functions that are continuous in V and V_∞. Using the chain rule and the generalized Green-Gauss theorem, we can rewrite this statement as

$$\int_V (\boldsymbol{\sigma}+\mathbf{m}) : \frac{\partial \mathbf{W}_u}{\partial x}\,dV + \int_V (\kappa_o \mathbf{E}+\mathbf{P})\cdot\frac{\partial W_\phi}{\partial \mathbf{x}}\,dV + \int_{V_\infty} \kappa_o \mathbf{E}\cdot\frac{\partial W_\phi}{\partial \mathbf{x}}\,dV$$
$$- \int_V \mathbf{f}\cdot\mathbf{W}_u\,dV - \int_{\partial V} \mathbf{T}\cdot\mathbf{W}_u\,dS - \int_{\partial V} \mathbf{n}\cdot\mathbf{m}^+\cdot\mathbf{W}_u\,dS + \int_V qW_\phi\,dV$$
$$+ \int_{\partial V+\Sigma} \omega W_\phi\,dS - \int_{\partial V} \kappa_o n\cdot\mathbf{E}^+ W_\phi\,dS = 0. \quad (25)$$

We approximate the field variables by the finite element interpolations,

$$\mathbf{u}(\mathbf{x}) \sim \mathbf{N}_u(\mathbf{x})\cdot\bar{\mathbf{u}} \quad \text{and} \quad \phi(\mathbf{x}) \sim \mathbf{N}_\phi(\mathbf{x})\cdot\bar{\boldsymbol{\phi}}. \quad (26)$$

In this equation $\bar{\mathbf{u}}$ and $\bar{\boldsymbol{\phi}}$ are vectors that contain the displacements and electric potential at a finite number of node points, and $\mathbf{N}_u$ and $\mathbf{N}_\phi$ are the associated shape functions for those nodes. The strain and electric field corresponding to the interpolated functions are computed from eqns (3), (21), and (26) as

$$\boldsymbol{\varepsilon} = \mathbf{B}_u\cdot\bar{\mathbf{u}} \quad \text{and} \quad \mathbf{E} = \mathbf{B}_\phi\cdot\bar{\boldsymbol{\phi}}. \quad (27)$$

Following a Galerkin approach, the weak statement can be approximately solved if in place of any functions $\mathbf{W}_u$ and W_ϕ, we prescribe the individual nodal shape functions, $\mathbf{N}_u$ and $\mathbf{N}_\phi$. The following set of discrete, nonlinear equations, that depend solely on the nodal values of the displacement and electric potential results:

$$\int_V (\mathbf{B}_u)^T\cdot(\boldsymbol{\sigma}+\mathbf{m})\,dV - \int_{\partial V} (\mathbf{N}_u)^T\cdot\mathbf{m}^+\cdot\mathbf{n}\,dS - \int_V (\mathbf{N}_u)^T\cdot\mathbf{f}\,dV - \int_{\partial V} (\mathbf{N}_u)\mathbf{T}\cdot T\,dS = \bar{\mathbf{F}}_u = 0 \quad (28)$$

and

$$-\int_V (\mathbf{B}_\phi)^T\cdot(\kappa_o\mathbf{E}+\mathbf{P})\,dV - \int_{V_\infty} \kappa_o(\mathbf{B}_\phi)^T\cdot\mathbf{E}\,dV + \int_V \mathbf{N}_\phi q\,dV$$
$$+ \int_{\partial V+\Sigma} \omega\mathbf{N}_\phi\,dV - \int_{\partial V_\infty} \kappa_o\mathbf{n}\cdot\mathbf{E}^+\mathbf{N}_\phi\,dS = \bar{\mathbf{F}}_\phi = 0. \quad (29)$$

The number of equations represented by eqns (28) and (29) is equal to the number of nodal field variables in the model. For convenience, we have defined the nodal residual vectors $\bar{\mathbf{F}}_u$ and $\bar{\mathbf{F}}_\phi$, which contain the right-hand sides of eqns (28) and (29) respectively.

The system of nonlinear eqns (28) and (29) is solved by successive iteration using a modified Newton method. If an approximate solution of $\bar{\mathbf{u}}^i$ and $\bar{\boldsymbol{\phi}}^i$ is known after iteration i, then by Newton's method, the corrections to the displacement, $\bar{\mathbf{c}}_u^{i+1}$, and electric potential, $\bar{\mathbf{c}}_\phi^{i+1}$, are given by the following linear system of equations:

$$\begin{bmatrix} \mathbf{K}_{uu}(\bar{\mathbf{u}}^i,\bar{\boldsymbol{\phi}}^i) & \mathbf{K}_{u\phi}(\bar{\mathbf{u}}^i,\bar{\boldsymbol{\phi}}^i) \\ \mathbf{K}_{\phi u}(\bar{\mathbf{u}}^i,\bar{\boldsymbol{\phi}}^i) & \mathbf{K}_{\phi\phi}(\bar{\mathbf{u}}^i,\bar{\boldsymbol{\phi}}^i) \end{bmatrix} \begin{bmatrix} \bar{\mathbf{c}}_u^{i+1} \\ \bar{\mathbf{c}}_\phi^{i+1} \end{bmatrix} = - \begin{bmatrix} \bar{\mathbf{F}}_u(\bar{\mathbf{u}}^i,\bar{\boldsymbol{\phi}}^i) \\ \bar{\mathbf{F}}_\phi(\bar{\mathbf{u}}^i,\bar{\boldsymbol{\phi}}^i) \end{bmatrix}. \quad (30)$$

$\mathbf{K}_{uu}$, $\mathbf{K}_{u\phi}$, $\mathbf{K}_{\phi u}$ and $\mathbf{K}_{\phi\phi}$ form the tangent stiffness matrix. By taking the derivatives of the residual vectors in eqns (28) and (29) with respect to the field variables, the components of the stiffness matrix are computed as shown in the next four equations:

$$\mathbf{K}_{uu} = \int_V (\mathbf{B}_u)^T : \frac{\partial \boldsymbol{\sigma}}{\partial \boldsymbol{\varepsilon}} : \mathbf{B}_u \, \mathrm{d}V, \tag{31}$$

$$\mathbf{K}_{u\phi} = \int_V (\mathbf{B}_u)^T : \left(\frac{\partial \boldsymbol{\sigma}}{\partial \mathbf{E}} + \frac{\partial \mathbf{m}}{\partial \mathbf{E}} \right) \cdot \mathbf{B}_\phi \, \mathrm{d}V - \int_{\partial V} (\mathbf{N}_u)^T \cdot \frac{\partial (\mathbf{m}^+ \cdot \mathbf{n})}{\partial \mathbf{E}} \cdot \mathbf{B}_\phi \, \mathrm{d}V, \tag{32}$$

$$\mathbf{K}_{\phi u} = -\int_V (\mathbf{B}_\phi)^T \cdot \frac{\partial \mathbf{P}}{\partial \boldsymbol{\varepsilon}} : \mathbf{B}_u \, \mathrm{d}V, \quad \text{and} \tag{33}$$

$$\mathbf{K}_{\phi\phi} = -\int_V (\mathbf{B}_\phi)^T \cdot \left(\kappa_o \mathbf{I} + \frac{\partial \mathbf{P}}{\partial \mathbf{E}} \right) \cdot \mathbf{B}_\phi \, \mathrm{d}V - \int_{V_\infty} \kappa_o (\mathbf{B}_\phi)^T \cdot \mathbf{B}_\phi \, \mathrm{d}V. \tag{34}$$

The exact tangent stiffness matrix represented by these equations is nonsymmetric due to the Maxwell stress terms in $\mathbf{K}_{u\phi}$. In our formulation we approximate the stiffness matrix with a symmetric matrix by replacing eqn (32) with the following equation:

$$\mathbf{K}_{u\phi} \sim \int_V (\mathbf{B}_u)^T : \frac{\partial \boldsymbol{\sigma}}{\partial \mathbf{E}} \cdot \mathbf{B}_\phi \, \mathrm{d}V. \tag{35}$$

In this sense our iteration scheme is a modified Newton method, not an exact Newton method. The partial derivatives of stress and polarization, with respect to strain and electric field, are determined from the individual constitutive models of the conductors and dielectrics.

The external electrical and mechanical loads are applied to the finite element model incrementally. In the iteration process for each increment, the field variables for iteration i, $\bar{\mathbf{u}}^i$ and $\bar{\boldsymbol{\phi}}^i$, are used to compute the corresponding state variables, $\mathbf{P}$ and $\boldsymbol{\sigma}$. These state variables are in turn used to calculate the residual vectors and tangent stiffness in eqn (30). The field variable corrections are computed from the linear system of equations, and added to $\bar{\mathbf{u}}^i$ and $\bar{\boldsymbol{\phi}}^i$ to obtain an improved approximation to the solution. This process continues until the residuals and corrections are within specified tolerances.

This algorithm for electromechanics was implemented in Martin Marietta's finite element program, FULCRUM. Two-dimensional, linear, isoparametric elements were created for plane stress, plane strain, and axisymmetric conditions. The **B**-bar method [Zienkiewicz and Taylor (1989)] was used in the plane strain and axisymmetric element formulations to prevent mesh "locking" caused by compressible or near-compressible material behavior.

4. CONSTITUTIVE MODEL FOR RELAXOR FERROELECTRIC CERAMICS

In this section, we examine the electromechanical behavior of a relaxor ferroelectric ceramic and present a phenomenological constitutive model developed by Hom and Shankar (1994) that approximates this behavior. Then, we incorporate that constitutive law into the nonlinear electromechanical finite element formulation presented in the previous section.

The electromechanical behavior of a typical multi-crystal relaxor ferroelectric near its Curie transition temperature is illustrated in Figs 2 and 3 [from Hom *et al.* (1994)]. The actual material (PMN-PT-BT) is a ternary system that contains 7.7% $PbTiO_3$ (PT) with $Pb(Mg_{1/3}Nb_{2/3})O_3$ (PMN) as the base and 2.5% $BaTiO_3$ (BT) as a dopant (percentages by volume). Figure 2 shows the measured dielectric behavior (induced polarization vs applied electric field) of PMN-PT-BT at 5°C under stress-free conditions. The electrically induced longitudinal strain vs applied electric field for a stress-free sample of PMN-PT-BT at 5°C is depicted in Fig. 3. At low fields, the induced strain is approximately proportional to the square of the electric field. However, higher-order electric field terms become significant at electric fields above 1MV/m.

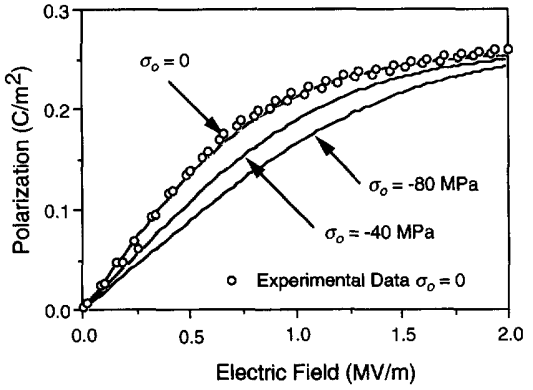

Fig. 2. The dielectric response of electrostrictive PMN-PT-BT at 5°C under various prestress loads σ_o. Discrete points denote experimental measurement, while the solid lines denote prediction by the Hom-Shankar constitutive model.

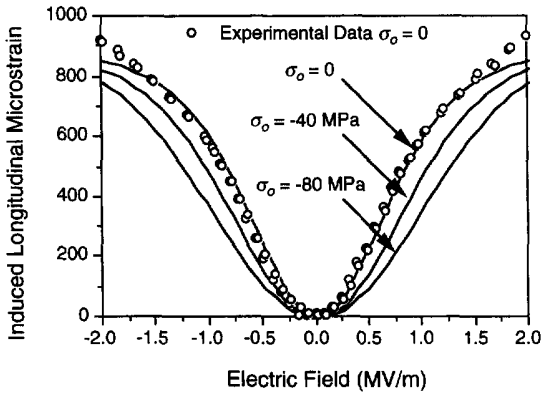

Fig. 3. The electrically induced strain response of electrostrictive PMN-PT-BT at 5°C under various prestress loads σ_o. Discrete points denote experimental measurement, while the solid lines denote prediction by the Hom-Shankar constitutive model.

The Hom-Shankar constitutive model approximates relaxor ferroelectric behavior by using polarization and strain as independent state variables. The model is based on four assumptions: (1) the ceramic has a multi-granular structure that results in isotropic behavior at the macroscopic level, (2) the electrically induced strain depends only on second-order polarization terms, (3) the elastic stiffness does not depend on polarization, and (4) the polarization saturates to a value P_s at high electric fields. With these assumptions, Hom and Shankar have derived an internal energy function for a relaxor ferroelectric of

$$U = \tfrac{1}{2}(\boldsymbol{\varepsilon}-\boldsymbol{\varepsilon}_E):\mathbf{C}:(\boldsymbol{\varepsilon}-\boldsymbol{\varepsilon}_E)+\frac{1}{2k}\left[|\mathbf{P}|\ln\left(\frac{P_{s^+}|\mathbf{P}|}{P_{s^-}|\mathbf{P}|}\right)+P_s\ln\left(1-\left(\frac{|\mathbf{P}|}{P_s}\right)^2\right)\right] \tag{36}$$

where the fourth order tensors $\mathbf{C}$ and $\mathbf{Q}$ are the isotropic elastic stiffness matrix and the isotropic electrostrictive strain coefficient matrix, respectively. k is a material constant, and the notation $|\mathbf{A}|$ represents the magnitude of the vector $\mathbf{A}$. $\boldsymbol{\varepsilon}_E$ is the polarization-induced strain given by

$$\boldsymbol{\varepsilon}_E = \mathbf{Q}:(\mathbf{P}\,\mathbf{P}) = (Q_{11}-Q_{12})\mathbf{P}\,\mathbf{P}+Q_{12}|\mathbf{P}|^2\mathbf{I} \tag{37}$$

where the coefficients, Q_{11} and Q_{12} are defined so that the longitudinal and transverse induced strains relative to the polarization direction are $Q_{11}|\mathbf{P}|^2$ and $Q_{12}|\mathbf{P}|^2$, respectively. The coefficients of matrix $\mathbf{C}$ depend only on Young's modulus, Y, and Poisson's ratio, ν, in the normal manner for linear isotropic elasticity.

Inserting eqn (36) into eqn (22), the mechanical behavior of a relaxor ferroelectric can be written as

$$\boldsymbol{\sigma} = \mathbf{C}:(\boldsymbol{\varepsilon} - \mathbf{Q}:(\mathbf{P}\,\mathbf{P})). \tag{38}$$

Similarly, the dielectric behavior of a relaxor ferroelectric can be derived from eqn (23) as

$$\mathbf{E} = -2(\boldsymbol{\varepsilon} - \mathbf{Q}:(\mathbf{P}\,\mathbf{P})):\mathbf{C}:\mathbf{Q}\cdot\mathbf{P} + \frac{1}{k}\operatorname{arctanh}\left(\frac{|\mathbf{P}|}{P_s}\right)\frac{\mathbf{P}}{|\mathbf{P}|}. \tag{39}$$

The first term in eqn (39) represents the converse electrostrictive effect, while the second term represents the stress-free dielectric behavior. This result can be rewritten in the more convenient form,

$$\mathbf{P} = P_s \tanh(k|\mathbf{R}|)\frac{\mathbf{R}}{|\mathbf{R}|}, \tag{40}$$

where we define $\mathbf{R}$ as

$$\mathbf{R} = \mathbf{E} + 2(\boldsymbol{\varepsilon} - \mathbf{Q}:(\mathbf{P}\,\mathbf{P})):\mathbf{C}:\mathbf{Q}\cdot\mathbf{P} = \mathbf{E} + 2\boldsymbol{\sigma}:\mathbf{Q}\cdot\mathbf{P}. \tag{41}$$

In order to implement the relaxor ferroelectric constitutive model into the finite element algorithm, we must establish a methodology for computing the state variables $\boldsymbol{\sigma}$ and $\mathbf{P}$, and the material stiffness derivatives required by eqns (31)–(35). Once these quantities are known, the tangent stiffness matrix and the nodal residual vector can be assembled. The constitutive calculations begin with the electric field and strain at a material point, which are directly computed in the finite element algorithm from the field variables of the previous Newton iteration. Using these values, eqn (40) is solved using Newton's method for the corresponding induced polarization. Then, the stress at the material point is computed from eqn (38) using this polarization and the strain state.

The Jacobian for the constitutive model can be derived from eqns (38) and (40). Differentiating the two equations yields

$$\mathrm{d}\boldsymbol{\sigma} = \mathbf{C}:\mathrm{d}\boldsymbol{\varepsilon} - 2\mathbf{C}:\mathbf{Q}\cdot\mathbf{P}\cdot\mathrm{d}\mathbf{P} \tag{42}$$

and

$$\mathrm{d}\mathbf{P} = \mathbf{H}\cdot[2(\boldsymbol{\varepsilon} - \mathbf{Q}:(\mathbf{P}\,\mathbf{P})):\mathbf{C}:\mathbf{Q} - 4(\mathbf{Q}\cdot\mathbf{P})^T:\mathbf{C}:\mathbf{Q}\cdot\mathbf{P}]\cdot\mathrm{d}\mathbf{P} + \mathbf{H}\cdot\mathrm{d}\mathbf{E} + 2\mathbf{H}\cdot(\mathbf{Q}\cdot\mathbf{P})^T:\mathbf{C}:\mathrm{d}\boldsymbol{\varepsilon} \tag{43}$$

where

$$\mathbf{H} = \mathrm{P}_s \tanh(k|\mathbf{R}|)\left[\frac{\mathbf{I}}{|\mathbf{R}|} - \frac{\mathbf{R}\,\mathbf{R}}{|\mathbf{R}|^3}\right] + \frac{kP_s\mathbf{R}\,\mathbf{R}}{\cosh^2(k|\mathbf{R}|)|\mathbf{R}|^2}. \tag{44}$$

Equation (43) can be manipulated to the form

$$\mathrm{d}\mathbf{P} = \mathbf{Z}\cdot\mathrm{d}\mathbf{E} + 2\mathbf{Z}\cdot(\mathbf{Q}\cdot\mathbf{P})^T:\mathbf{C}:\mathrm{d}\boldsymbol{\varepsilon}, \tag{45}$$

where

$$\mathbf{Z} = [\mathbf{I} - \mathbf{H}\cdot[2(\boldsymbol{\varepsilon} - \mathbf{Q}:(\mathbf{P}\,\mathbf{P})):\mathbf{C}:\mathbf{Q} - 4(\mathbf{Q}\cdot\mathbf{P})^T:\mathbf{C}:\mathbf{Q}\cdot\mathbf{P}]]^{-1}\cdot\mathbf{H}. \tag{46}$$

Inserting eqn (45) into eqn (42) gives

Table 1. Material constants for PMN-PT-BT at 5°C

Y (GPa)	ν	Q_{11} (m^4/C^2)	Q_{12} (m^4/C^2)	P_s (C/m^2)	k (m/MV)
115	0.26	1.33×10^{-2}	-6.06×10^{-3}	0.2589	1.16

$$d\boldsymbol{\sigma} = [\mathbf{C} - 4\mathbf{C}:\mathbf{Q}\cdot\mathbf{P}\cdot\mathbf{Z}\cdot(\mathbf{Q}\cdot\mathbf{P})^T:\mathbf{C}]:d\boldsymbol{\varepsilon} - 2\mathbf{C}:\mathbf{Q}\cdot\mathbf{P}\cdot\mathbf{Z}\cdot d\mathbf{E}. \tag{47}$$

The combination of eqn (45) and eqn (47) define the Jacobian by

$$\begin{bmatrix} d\boldsymbol{\sigma} \\ d\mathbf{P} \end{bmatrix} = \begin{bmatrix} \mathbf{C} - 4\mathbf{C}:\mathbf{Q}\cdot\mathbf{P}\cdot\mathbf{Z}\cdot(\mathbf{Q}\cdot\mathbf{P})^T:\mathbf{C} & -2\mathbf{C}:\mathbf{Q}\cdot\mathbf{P}\cdot\mathbf{Z} \\ 2\mathbf{Z}\cdot(\mathbf{Q}\cdot\mathbf{P})^T:\mathbf{C} & \mathbf{Z} \end{bmatrix} \cdot \begin{bmatrix} d\boldsymbol{\varepsilon} \\ d\mathbf{E} \end{bmatrix}. \tag{48}$$

In the finite element algorithm, the Jacobian at a material point is directly computed from eqn (48) using the state of strain, electric field, and polarization. This Jacobian leads to a symmetric tangent stiffness matrix due to the individual symmetry of **C** and **Z**.

The material constants Y, ν, Q_{11}, Q_{12}, P_s and k in the relaxor ferroelectric model must be measured using the electrical and mechanical tests described by Hom *et al.* (1994). The constants for PMN-PT-BT at 5°C measured by Hom *et al.* are tabulated in Table 1. Using these values, the electromechanical response of the constitutive model at various levels of uniaxial prestress σ_o were predicted and plotted as solid lines in Figs 2 and 3. The prestress is applied in the same direction as the electric field. At moderate fields, ~1MV/m, the model predicts a significant drop in polarization due to coupling with the compressive prestress; however the polarization approaches the same asymptotic value with larger fields, >2MV/m, regardless of the level of prestress. A comparison with the experimentally measured response shows that the Hom and Shankar model represents stress-free behavior even at high electric fields. Further experiments are currently being conducted to compare the model with measurements made under compressive prestress.

5. SOLUTION FOR A MULTILAYERED ELECTROSTRICTIVE ACTUATOR

In order to demonstrate our finite element formulation, we analyzed a multilayered ceramic actuator with internal tab electrodes described by Winzer *et al.* (1989). Yang and Suo (1994) have also studied this configuration using analytical methods, and their results are compared with our numerical analysis. In our model, the dielectric portion of the actuator is constructed from the PMN-PT-BT material described in the previous section.

Shown in Fig. 4, multilayered actuators comprise thin electrostrictive ceramic layers sandwiched between alternating positive and negative plate electrodes. The active ceramic

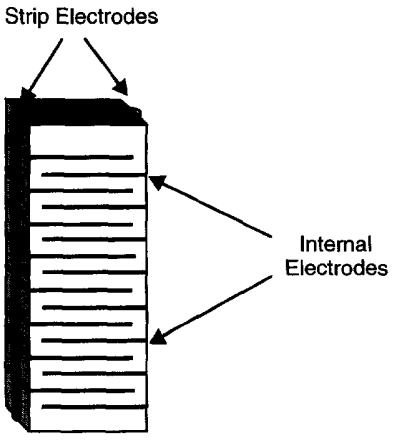

Fig. 4. Configuration of a multilayered ceramic actuator with alternating electrodes.

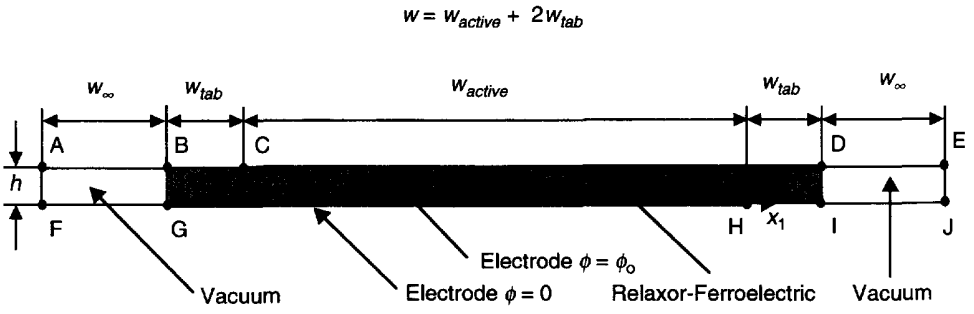

Fig. 5. Cell model of a single layer that approximates the multilayer ceramic actuator.

layers are electrically in parallel and mechanically in series, so significant induced displacement is possible with relatively low voltages. The positive and negative electrodes are addressed by an interconnecting strip electrode on either side of the actuator. In a tab configuration, electrodes do not extend completely to the opposing edge in order to isolate them from the other strip electrode. This configuration is considerably easier to manufacture than a configuration in which each plate electrode is addressed by an individual interconnection. The electrically active region exists in the portions of the actuator where the positive and negative electrodes overlap, while an electrically inactive region, or tab, exists on both sides of the actuator. Voltages are applied to the device that typically result in a nominal electric field of 0.4 to 1.5MV/m in the active region. When the electrodes are charged, the two tab regions resist the expansion of the active layer and create tensile stresses in the ceramic. Electromechanical modeling is necessary to predict both the induced displacement and the stress state of the actuator device.

Boundary value problem

In our analysis of the multilayered actuator, we studied a two-dimensional unit cell consisting of a single ceramic layer, two opposing electrodes, and the neighboring vacuum, as shown in Fig. 5. The top electrode extends from points C to D in the figure (surface ∂V_{CD}), while the bottom electrode extends from points G to H (surface ∂V_{GH}). Conditions of symmetry were applied to the top and bottom faces of the cell, so the model simulated a linear array of cells extending along the axis of the actuator. While this approach actually models an infinitely long actuator, the cell should adequately model the electromechanical state of a layer near the center of the actuator stack.

The Cartesian coordinate system used in the analysis and the key dimensions of the cell model are illustrated in Fig. 5. For convenience we have defined the origin of the coordinate system as the right tip of the bottom electrode. w and h are the total width of the actuator and the height of a single ceramic layer, respectively. w_{active} denotes the width of the active portion, and w_{tab} denotes the width of the tab regions. The two vacuum regions surrounding the actuator should extend to infinity, however for our numerical model, we have artificially truncated those regions a distance w_∞ from the side of the actuator. Table 2 lists the cell dimensions used in our calculations.

The only electric charge in the cell lies on the two conducting plate electrodes, the dielectric layer itself does not contain any distributed volume charge. Therefore, q equals zero on V_{BDIG}. The electrodes are only 3–5 μm thick so they were not modeled explicitly with a group of finite elements. Instead, the top electrode is represented on surface ∂V_{CD} by applying a voltage ϕ_o directly to the adjoining dielectric. In a similar fashion, the voltage on the surface ∂V_{GH} was set to zero to simulate the grounded bottom electrode.

Table 2. Cell dimensions for the finite element analysis of a multilayered actuator

w	h	w_{active}	w_{tab}	w_∞
6 mm	115 μm	5.59 mm	205 μm	575 μm

On the top of the cell, a uniform axial displacement U was applied and the shear tractions were zero. Therefore, the complete boundary conditions for the top surface can be expressed by the following equations

$$\omega = 0, \quad \mathbf{n}\cdot\mathbf{E}^{+} = 0, \quad u_2 = u_o, \quad T_1 = 0 \quad \text{on } \partial V_{BC}, \tag{49}$$

$$\phi = \phi_o, \quad u_2 = u_o, \quad T_1 = 0 \quad \text{on } \partial V_{CD}. \tag{50}$$

On the bottom side of the cell, the axial displacements are fixed and the shear tractions are zero. Therefore, the equations boundary conditions for the bottom can be written:

$$\phi = 0, \quad u_2 = 0, \quad T_1 = 0 \quad \text{on } \partial V_{GH}, \tag{51}$$

$$\omega = 0, \quad \mathbf{n}\cdot\mathbf{E}^{+} = 0, \quad u_2 = 0, \quad T_1 = 0 \quad \text{on } \partial V_{HI}. \tag{52}$$

The sides of the actuator are free of mechanical stress, so $\mathbf{T}$ equals zero on ∂V_{BG} and ∂V_{DI}. The average prestress on the actuator T_{avg} is given by

$$T_{avg} = \int_{\partial V_{BC}+\partial V_{CD}} T_2 \, \mathrm{d}S = -\int_{\partial V_{GH}+\partial V_{HI}} T_2 \, \mathrm{d}S. \tag{53}$$

The symmetry conditions on the top and bottom of the two vacuum regions require that $\mathbf{n}\cdot\mathbf{E}^{+}$ equals zero on ∂V_{AB}, ∂V_{FG}, ∂V_{DE} and ∂V_{IJ}. On the surfaces ∂V_{AF} and ∂V_{EJ}, boundary conditions must be applied that simulate radiation into the remainder of the infinite domain. These conditions can be modeled with infinite elements or by coupling the finite elements to a boundary integral element formulation [Jin (1993)]. However, we assumed that the two surfaces have a uniform electric field, a situation that occurs when w_∞ is sufficiently large. Since the two electrodes have equal charges with opposite sign, the total charge in the cell is zero. Therefore, Gauss's law shows that $\mathbf{n}\cdot\mathbf{E}^{+}$ equals zero on ∂V_{AF} and ∂V_{EJ}.

The finite element mesh used to solve this boundary value problem is shown in Fig. 6. The mesh consists of 3608 four-noded, isoparametric electromechanical elements for the actuator and 192 four-noded, isoparametric electrostatic elements for the surrounding vacuum. The model had a total of 4137 nodes.

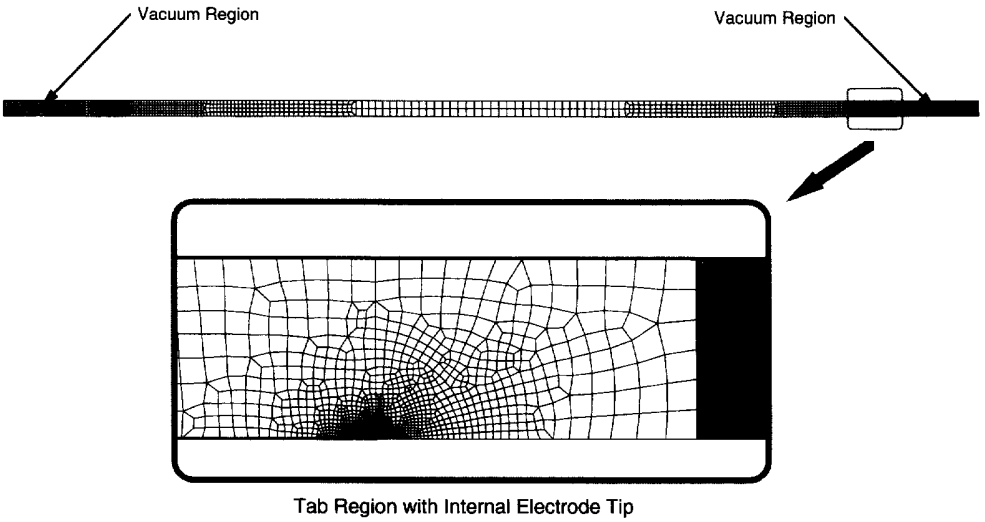

Fig. 6. The finite element mesh used to solve the boundary problem of an electrostrictive multilayered actuator.

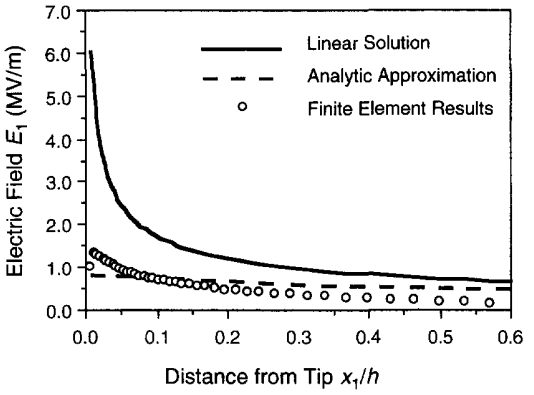

Fig. 7. Comparison of E_1 ahead of the electrode tip predicted by the nonlinear electrostrictive finite element results, the analytical solution presented in Appendix B and the linear dielectric solution for $E_o = 1.0$ MV/m.

Numerical results

Calculations were performed for the multilayered actuator cell model with nominal electric fields ($E_o = -\phi_o/h$) of 0.5, 1.0 and 1.5MV/m, and T_{avg} equal to zero. Our results are compared with a new analytical approximation of the internal electrode problem, which is presented in Appendix B. The analytical approximation assumes that electro-mechanical variables are only partially coupled, and the dielectric response is perfectly saturating. In addition, we assume that the saturated polarization region surrounding the electrode tip is in turn surrounded by the singular electric field for a linear dielectric (i.e. small-scale saturation). However, even with these assumptions, the analytical solution still retains the salient features observed in the finite element results.

The electric field components ahead of and behind the electrode tip for $E_o = 1.0$MV/m are plotted in Figs 7 and 8. The discrete points represent the finite element results. As expected, a singularity exists at the electrode tip. The two figures also depict the singular portion of the electric field computed from linear dielectric analysis (i.e. Laplace's equation). Yang and Suo (1994) have shown that this linear field is

$$[E_1, E_2] = \sqrt{\frac{h}{\pi r}} E_o[\cos(\theta/2), \sin(\theta/2)], \tag{54}$$

where r and θ are the cylindrical coordinates of a material point relative to the tip. Our numerical analysis indicates that the electric field is radically changed by the ceramic's nonlinear dielectric response. The field behind the tip is significantly higher than the

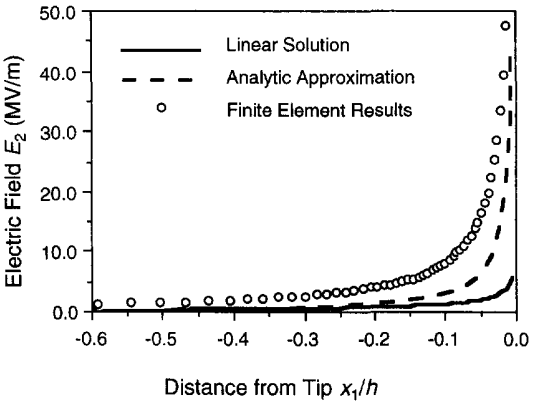

Fig. 8. Comparison of E_2 behind the electrode tip predicted by the nonlinear electrostrictive finite element results, the analytical solution presented in Appendix B and the linear dielectric solution for $E_o = 1.0$ MV/m.

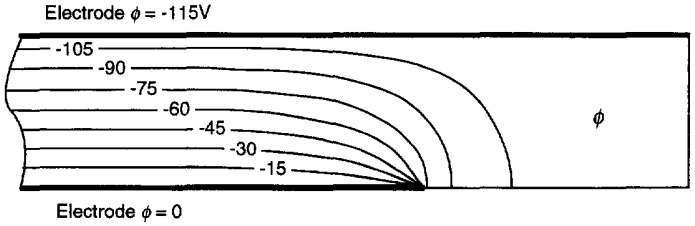

Fig. 9. A contour plot of the electric potential ϕ (V) in the near-electrode tip region for E_o = 1.0 MV/m.

corresponding field computed via Laplace's equation. The non-linear analytic solution presented in Appendix B predicts the electric field behind the tip is

$$E_2 = \sqrt{\frac{hR}{\pi}}\frac{E_o}{r}. \tag{55}$$

This analytical result is also plotted in Fig. 8. The finite element results also predict a r^{-1} order singularity, however, the magnitude is 120% higher than the analytical result. Ahead of the electrode tip, the electric fields predicted by the both the finite element and non-linear closed-form solutions are lower than the corresponding field predicted by the Laplace's equation.

A contour plot of ϕ in the tab region on cell's right side is displayed in Fig. 9 for E_o = 1.0MV/m. The plot shows that the lines of constant potential behind the electrode tip are focused into the tip in a centered fan shape. This agrees qualitatively with the non-linear analytical result (see Fig. B2) which predicts that the constant potential lines in the saturated zone behind the electrode tip are straight and centered at the tip.

Figure 10 is a contour plot of $|\mathbf{P}|$ near the electrode tip on the right side of the cell at E_o = 1.0MV/m. The plot reveals that the high nonlinear electric fields create a region of saturated polarization behind the electrode tip and a sharp polarization gradient directly ahead of the tip. The stress-free polarization that corresponds to E_o = 1.0MV/m is 0.821 P_s. Clearly the plot shows that the polarization magnitude in the bulk of the active region is below this value. This drop in polarization is due to the 4MPa compressive stress in the active portion created by the constraint of the inactive tab region. The finite element results qualitatively agree with the non-linear analytical solution presented in Appendix B, which predicts that the saturated zone is circular in shape and perched directly behind the electrode tip. However, the diffuse saturation zone shown in Fig. 10 is oval in shape, in contrast to the perfectly saturated analytical results. This shape difference results from the non-singular electric field terms which are present in the finite element calculations, but are ignored in the analytical solution. For E_o = 1.0MV/m, the analytical solution predicts that the radius of the saturation zone is 0.428h. The diffuse zone computed by the finite element analysis is smaller, however, its dimensions are still significant when compared to the characteristic length h. Consequently, it appears that small-scale saturation conditions do not exist at the electrode tip for this level of applied electric load.

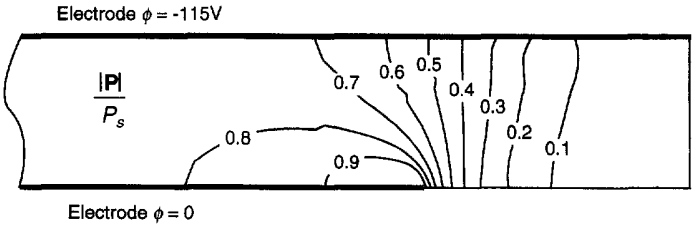

Fig. 10. A contour plot of the normalized polarization magnitude ($|\mathbf{P}|/P_s$) in the near-electrode tip region for E_o = 1.0 MV/m.

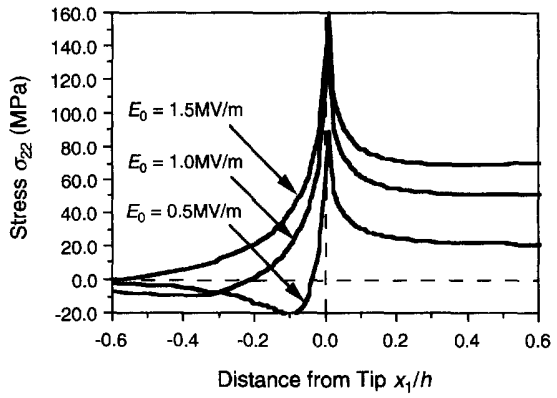

Fig. 11. The stress σ_{22} (MPa) ahead and behind the electrode tip for various electric loads.

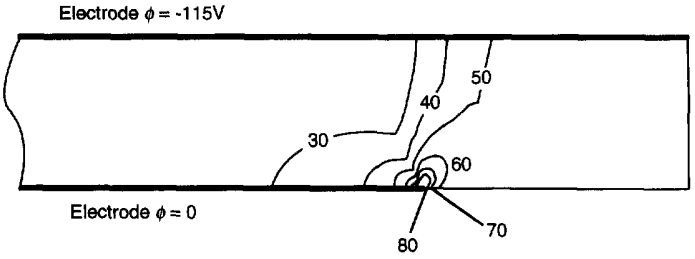

Fig. 12. A contour plot of the maximum principal stress (MPa) near the electrode tip for E_o = 1.0 MV/m.

Figure 11 displays the normal stress, σ_{22}, along the electrode plane for three different nominal electric fields, while Fig. 12 plots the contours of maximum principal stress in the near tip region for E_o = 1.0 MV/m. As suggested by Winzer *et al.* (1989), the finite element calculations also predict high tensile stresses (20–80MPa) in the bulk of the tab region due to the electrostrictive strains in the neighboring active region. A relatively low σ_{22} compressive stress in the active region keeps the layer in equilibrium. The plane strain constraint creates a tensile σ_{33}, so the maximum principal stress is tensile even in the active region. Both Figs 11 and 12 clearly show that the electrode tip is a stress singularity even though the near tip induced strains are finite. The analytical solution presented in Appendix B also predicts a stress singularity at the electrode tip of

$$\sigma_{22} = -\frac{(Q_{11}-Q_{12})P_s^2 Y}{4(1-\nu^2)}\ln r, \tag{56}$$

where the magnitude of the $\ln r$ singularity does not depend on E_o. Using the material constants in Table 1, the magnitude of the $\ln r$ stress term in (56) is -39.9 MPa. Figure 13 plots the finite element predictions for σ_{22} behind the electrode tip versus $\ln(-x_1/h)$. This figure shows that the singularity observed in the finite element calculations is also a $\ln r$ type. Using Fig. 13, the magnitude of the $\ln r$ stress singularity is -30.4, -32.4 and -32.6 MPa for E_o = 0.5, 1.0 and 1.5 MV/m, respectively. The average magnitude predicted by the finite element results is 20% lower than the value predicted by the analytical approximation. Like the analytical solution, the magnitude of the singularity predicted by the finite element results does not appear to depend on the applied field. Increasing the appled electric load only increases the magnitude of the non-singular stress terms.

Crack propagation

The finite element results indicate that electrode tips are a potential site for crack growth and failure. Indeed, Furuta and Uchino (1993) have observed crack nucleation and subsequent stable growth from an electrode tip in a multilayered piezoelectric actuator

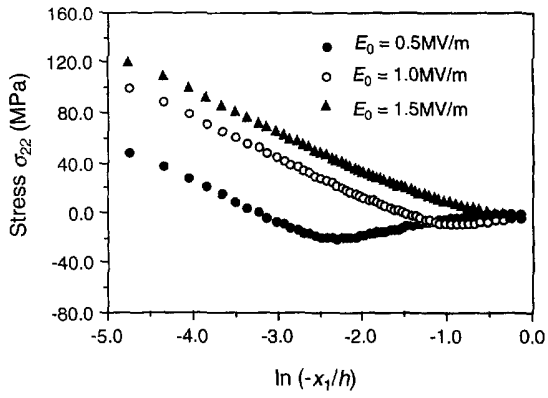

Fig. 13. Plot of σ_{22} (MPa) behind the electrode tip vs the natural log of distance from the tip.

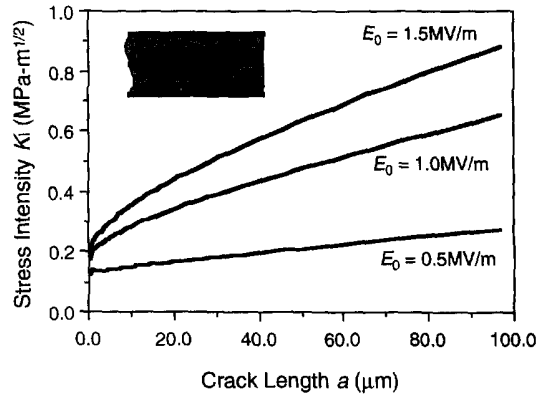

Fig. 14. The predicted stress intensity factors for a crack nucleating from the electrode tip for various levels of electric load. The inset shows the crack geometry.

during operation. Following the method of Yang and Suo (1994), the near-tip stress state of the finite element analysis was used to approximate the stress intensity factors for this type of crack and assess the actuator's reliability. Shown in the insert of Fig. 14, the crack is parallel to the electrodes, and its length is a. In our analysis, the pure elastic problem of a crack with pressure equal to the magnitude of σ_{22} shown in Fig. 11 is superimposed with the electrostriction problem without a crack as solved by the finite element analysis. Like Yang and Suo, we assume that (1) the stresses of the pressurized crack problem do not affect the near-tip electric field, (2) the electric charge from the electrode tip does not migrate into the crack faces, and (3) the finite boundaries of the cell do not affect the near-tip stresses of the pressurized crack problem.

The resulting stress intensity factors vs crack length for $E_o = 0.5$, 1.0, and 1.5 MV/m appear in Fig. 14. For all three cases, the initial stress intensity factor is $\sim$0.2MPa-m$^{1/2}$. The calculations also indicate that once the crack nucleates it should experience unstable growth as a result of the high tensile stress in the tab region. However, Friedman and White (1994) have measured the fracture toughness of PMN-PT as 0.9MPa-m$^{1/2}$ using indentation techniques, so it appears that this model does not predict the spontaneous nucleation and subsequent stable growth observed by Furuta and Uchino.

6. DISCUSSION

The finite element method presented in this paper models electrostrictive behavior in ceramic actuators and sensors. Unlike previous analysis techniques, this method accounts for full, nonlinear coupling between the electric field and the material's stress state. Coupling

occurs at two levels: through the electric body forces due to distributed charges in the ceramic, and through the electrostrictive constitutive behavior of the ceramic itself.

The fully coupled finite element technique has been demonstrated on multilayered electrostrictive actuators. The results of our analysis show that significant deviation from the linear dielectric solution for these devices [Yang and Suo (1994)] occurs due to the non-linear response of the relaxor ferroelectric. In particular, the finite element results predict (1) a r^{-1} order electric field singularity in the saturated region behind the internal electrode tip, and (2) a $\ln r$ stress singularity at the electrode tip. The last result was particularly interesting since the induced electric strain saturates to a finite value at the tip.

In order to verify the finite element results, a new analytic solution for an internal electrode in a perfectly saturating dielectric is presented in Appendix B. The analytic solution qualitatively agrees with the numerical calculations, since it also yields a r^{-1} singularity in an electric field and a $\ln r$ singularity in stress. In addition, both solutions predict that the saturation zone develops behind the electrode tip. However, the magnitude of the electric field singularity is 120% greater for the finite element calculations when compared to the closed-form solution. This discrepancy is most likely due to the assumptions of small-scale saturation used in the analytical model. In our solution, the magnitude of the r^{-1} singularity in the saturation zone is determined from the surrounding electric field given by eqn (54). However, the radius of the zone predicted by the closed-form solution is $0.428h$ at $E_o = 1.0$ MV/m. The finite element calculations at that electric load also predict a diffuse zone size of the same order of h. Consequently, conditions of small-scale non-linearity do not exist at the electrode tip. The order of the electric field singularity is still r^{-1} for large-scale saturation, but its magnitude must be determined analytically by methods that account for full saturation of the layer. Since the finite element calculation models the fully or near-fully saturated conditions numerically, the singularity's magnitude computed by our numerical analysis should be more accurate than the analytical result.

Both the finite element and analytical results predict a $\ln r$ singularity at the internal electrode tip. The magnitude of the singularity observed in the finite element computations is 20% lower than the magnitude computed via the analytical solution. However, the closed-form approximation assumes that the active region of the actuator is fully saturated everywhere behind the electrode tip. This assumption will lead to a higher stress concentration factor when compared to a finite element results, since the numerical calculation features a diffuse saturation zone. In summation, the non-linear analytical solution qualitatively validates the finite element results for the multilayered actuator problem.

Yang and Suo (1994) have also studied the stress field near an internal electrode tip in a material with saturating polarization. In their analysis, they assumed that small-scale saturation occurs at the tip and the electric field is unchanged by the saturating polarization in both the saturation region and the surrounding material. Therefore their model's electric field is described by linear dielectric field of (54). Using that equation, Yang and Suo reasoned that the saturation region is a circle centered at the electrode tip with a radius defined by a critical electric field. Inside the saturation zone, the induced strain is

$$\varepsilon_E = P_s^2 \mathbf{Q} : \left(\frac{\mathbf{E}}{|\mathbf{E}|} \frac{\mathbf{E}}{|\mathbf{E}|} \right). \tag{57}$$

where $\mathbf{E}$ is defined by (54). Outside the zone, the induced strain is zero. Yang and Suo predicted that the stresses in the electrode tip were finite using this induced strain field in contrast to our results. We believe that our analytical solution is more complete than the Yang and Suo solution, since we actually compute the electric field for a perfectly saturating polarization. Our results show that the saturation zone and electric field are significantly modified by the non-linear dielectric response of the relaxor ferroelectric. Indeed, the saturation zone is not centered at the electrode tip, but positioned directly behind it. These results appear to invalidate Yang and Suo's initial assumption that the electric field given by solution of Laplace's equation is unperturbed by a saturating polarization.

Finally we note that our fracture mechanics analysis of crack growth was performed by superimposing the finite element results on to an elastic crack of finite length. While this approximation is consistent with the fracture analysis performed by Yang and Suo for internal electrodes, an improved analysis would explicitly model the crack in the finite element mesh with various lengths. Those type calculations would model any perturbation in the coupled electric field and stress state introduced by the presence of the crack. We are currently undertaking this fracture mechanics task and will report on the results in a future paper.

Acknowledgement—This work was supported by the Smart Materials and Synthesis Program established under the Advance Research Projects Agency (ARPA) Agreements Authority (Agreement no. MDA972-H-003) and monitored by Dr Robert Crowe. The authors would like to thank Dr Frank Crowne of Martin Marietta Laboratories for several helpful discussions concerning the analytical work presented in Appendix B.

REFERENCES

Abe, K., Uchino, K. and Nomura, S. (1986). Barium titanate-based actuator with ceramic internal electrodes. *Ferroelectrics* **68,** 215–223.

Allik, H. and Hughes, T. J. R. (1970). Finite element method for piezoelectric vibrations. *Int. J. Num. Meth.* **2,** 151–157.

Allik, H., Webman, K. M. and Hunt, J. T. (1974). Vibrational response of sonar transducers using piezoelectric finite elements. *J. Acoust. Soc. Am.* **56,** 1782–91.

Böttcher, C. J. F. (1952). *Theory of Electric Polarization*, Elsevier Publishing Company, Amsterdam, pp. 36–41.

Cross, L. E. (1987). Relaxor ferroelectrics. *Ferroelectrics* **76,** 241–67.

Eringen, A. C. (1963). On the foundations of electrostatics. *Int. J. Engng Sci.* **1,** 127–153.

Friedman, S. W. and White, G. S. (1994). Intelligent ceramic materials: issues of brittle fracture. In *Proceedings of the Second International Conference on Intelligent Materials* (Edited by C. A. Rodgers and G. G. Wallace), Williamsburg, Virgina, 5–8 June, 1994, pp. 52–62.

Furuta, A. and Uchino, K. (1993). Dynamic observation of crack propagation in piezoelectric multilayer actuators. *J. Am. Ceram. Soc.* **76,** 1615–1617.

Gandhi, M. V. and Thompson, B. S. (1992). *Smart Materials and Structures*. Chapman and Hall, London, pp. 105–135.

Hom, C. L., Pilgrim, S. M., Shankar, N., Bridger, K., Massuda, M. and Winzer, S. R. (1994). Calculation of quasi-static electromechanical coupling coefficients for electrostrictive ceramic materials. *IEEE Trans. on Ultrason., Ferroelec., Freq. Contr.* **41,** 542–551.

Hom, C. L. and Shankar, N. (1994). A fully coupled constitutive model for electrostrictive ceramic materials. *J. Intell. Mater. Syst. and Struct.* **5,** 795–801.

Hult, J. A. H. and McClintock, F. A. (1956). Elastic-plastic stress and strain distribution around sharp notches under repeated shear. In *Proceedings of the Ninth International Congress of Applied Mechanics*, Vol. 8, University of Brussels, Belgium, pp. 51–58.

Jin, J. (1993). *The Finite Element Method in Electromagnetics*, John Wiley and Sons, New York, pp. 281–352.

Kagawa, Y. and Yamabuchi, T. (1974). Finite element simulation of two-dimensional electromechanical resonators. *IEEE Trans. Sonics Ultrason.* **21,** 275–283.

Kirkby, C. T. (1981). Electrostriction and strain-optic phenomena in PLZT 9/65/35. *Ferroelectrics* **37,** 567–570.

Kuwata, J., Uchino, K. and Nomura, S. (1980). Electostrictive coefficients of $Pb(Mg_{1/3}, Nb_{2/3})O_3$ ceramics. *Jpn. J. Appl. Phys.* **19,** 2099–2103.

Landau, L. D. and Liftshitz, E. M. (1960). *Electrodynamics of Continuous Media.*, Pergamon Press, Oxford.

McMeeking, R. M. (1987). On mechanical stresses at cracks in dielectrics with application to dielectric breakdown. *J. Appl. Phys.* **62,** 3116–22.

McMeeking, R. M. (1989). Electrostrictive stress near crack like flaws. *J. Appl. Math. Phys.* **40,** 615–27.

Pilgrim, S. M., Massuda, M., Prodey, J. D. and Ritter, A. P. (1992). Electromechanical properties of some $Pb(Mg_{1/3}Nb_{2/3})O_3$-$PbTiO_3$-$(Ba,Sr)TiO_3$ ceramics: I. *J. Am. Ceram. Soc.* **75,** 1964–1649.

Somolenski, G. A., Isupov, V. A., Agranovskaya, A. I. and Poror, S. N. (1961). Ferroelectrics with diffuse phase transitions. *Soviet Physics of Solid State (English Translation)* **2,** 2584–2594.

Taylor, D. J., Newnham, R. E. and Carlson, W. B. (1988). The effect of electric field on mechanical strain and stress in flawed electroceramics. *Ferroelectrics* **87,** 81–84.

Toupin, R. A. (1956). The elastic dielectric. *J. Rational Mech. Anal.* **5,** 849–915.

Toupin, R. A. (1963). A dynamical theory of elastic dielectrics. *Int. J. Engng Sci.* **1,** 101–126.

Uchino, K. (1986). Electrostrictive actuators: materials and applications. *Ceramic Bull.* **65,** 647–652.

Uchino, K., Nomura, S., Cross, L. E., Jang, S. J. and Newnham, R. E. (1980). Electrostrictive effect in lead magnesium niobate single crystals. *J. Appl. Phys.* **51,** 1142–1145.

Voight, W. (1910). *Lehrbuch der Kristallphysik*, Leipzig.

Winzer, S. R., Shankar N. and Ritter, A. P. (1989). Designing cofired multilayered electrostrictive actuators for reliability. *J. Amer. Ceram. Soc.* **72,** 2246–2257.

Yang, W. and Suo, Z. (1994). Cracking in ceramic actuators caused by electrostriction. *J. Mech. Phys. Solids* **42,** 649–663.

Zienkiewicz, O. C. and Taylor, R. L. (1989). *The Finite Element Method: Volume* 1: *Basic Formulation and Linear Problems*. McGraw-Hill, London, pp. 206–59.

APPENDIX A: GENERALIZED GREEN-GAUSS THEOREM

In this Appendix, we derive a generalized Green-Gauss theorem for vector field **A** that is distributed in the dielectric-conductor composite shown in Fig. 1. In this proof we assume that the field is continuous thoughout V except for the surfaces ∂V and Σ. The normal Green-Gauss theorem,

$$\int_{V_i}\left(\frac{\partial}{\partial x}\right)\cdot\mathbf{A}\,dV=\int_{\partial V_i}\mathbf{n}_i\cdot\mathbf{A}\,dS \tag{A1}$$

is still valid where V_i is any continuous subregion of V that does not contain discontinuities of **A**, ∂V_i is the surface that encloses V_i, and $\mathbf{n}_i$ is the outward normal of ∂V_i. If we let the subregions V_i represent the individual dielectric and conducting components of the composite, then summing eqn (A1) for each V_i yields,

$$\int_{V}\left(\frac{\partial}{\partial \mathbf{x}}\right)\cdot\mathbf{A}\,dV=\sum_i\int_{\partial V_i}\mathbf{n}_i\cdot\mathbf{A}\,dS. \tag{A2}$$

The area of integation for the right-hand side of equation (A2) equals the interior of ∂V plus both the interior and exterior of Σ. We note that $\mathbf{n}_i$ on the interior of Σ equals $-\mathbf{n}$, and $\mathbf{n}_i$ on the exterior of Σ equals $\mathbf{n}$. Therefore, the right-hand side of the equation can be rewritten as

$$\sum_i\int_{\partial V_i}\mathbf{n}_i\cdot\mathbf{A}\,dS=\int_{\partial V}\mathbf{n}\cdot\mathbf{A}^-\,dS+\int_{\Sigma}(\mathbf{n}\cdot\mathbf{A}^+-\mathbf{n}\cdot\mathbf{A}^-)\,dS. \tag{A3}$$

Combining eqns (A2) and (A3), and $[\![\mathbf{A}]\!]=\mathbf{A}^+-\mathbf{A}^-$, we obtain

$$\int_{\partial V}\mathbf{n}\cdot\mathbf{A}^+\,dS=\int_{V}\left(\frac{\partial}{\partial \mathbf{x}}\right)\cdot\mathbf{A}\,dV+\int_{\partial V+\Sigma}\mathbf{n}\cdot[\![\mathbf{A}]\!]\,dS, \tag{A4}$$

which is the generalized Green-Gauss's theorem for the region V.

APPENDIX B: AN ANALYTIC APPROXIMATION FOR THE ELECTRIC FIELD AND STRESS STATE NEAR AN INTERNAL ELECTRODE

In this Appendix, we present an analytic solution for the electro-mechanical state near a multilayered actuator's internal electrodes. The purpose of this solution is to verify the finite element results presented in the main text of the paper. In particular, the closed-form solution must predict (1) the strong electric field singularity behind the electrode tip and (2) the stress singularity at the electrode tip observed in the finite element results. Our analysis uses a simplified constitutive law for the relaxor ferroelectric, however the solution still retains the essential features predicted by the finite element analysis. Our approach assumes that the electro-mechanical problem is only partially coupled. The electrostatic field is first solved for a non-linear dielectric response without mechanical coupling. The elastic stress state at the electrode tip is then computed using the mechanical constitutive eqn (38) with the analytically computed polarization field.

For simplicity, we approximated the polarization response of the ferroelectric as linear dielectric-perfectly saturated as shown in Fig. B1. The linear dielectric permittivity is P_sk and the saturation polarization is P_s. This simple model idealizes the stress-free polarization response (Fig. 2) used in the finite element calculations. Using polar coordinates (r, θ) centered at the electrode tip, the polarization in the saturation zone is

$$P_r^2+P_\theta^2=P_s^2. \tag{B1}$$

First, we assume that the product of electric field and free space permittivity is small compared to the saturation polarization (for the PMN values given in the main text the electric field must be order 1 GV/m for this product to be significant). With this assumption, Gauss's law (7) reduces to

$$\frac{1}{r}\frac{\partial(rP_r)}{\partial r}+\frac{1}{r}\frac{\partial P_\theta}{\partial\theta}=0. \tag{B2}$$

(B1) and (B2) form the complete governing equations for the saturation region. For the internal electrode problem, the solution to this equation is completely analogous to the solution of Hult and McClintock (1956) for an elastic–perfectly plastic, anti-plane shear crack. The saturated zone is circle of radius R which is perched directly behind the electrode tip. For convenience we introduce the polar coordinates $(\bar{r}, \bar{\theta})$ with an origin at the center of the

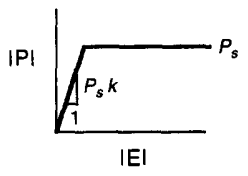

Fig. B1. Idealized dielectric behavior for the relaxor ferroelectric used in the analytical solution.

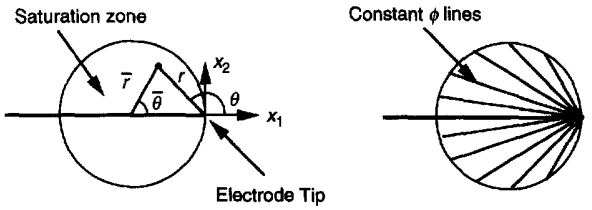

Fig. B2. Saturated zone shape and constant potential lines for the electrical solution of an internal electrode.

saturation zone as shown in Fig. B2. Outside the saturation zone the electric field is the singular field for linear dielectric behavior given by (54), but now centered at $\bar{r} = 0$ not $r = 0$. Inside the saturation zone, the solution that satisfies (B1), (B2) and the boundary conditions is

$$P_\theta = -P_s, \quad P_r = 0 \quad \text{for} \frac{\pi}{2} < \theta < \pi \quad \text{and}$$

$$P_\theta = P_s, \quad P_r = 0 \quad \text{for} \quad -\pi < \theta < -\frac{\pi}{2}. \tag{B3}$$

This polarization leads to an electric field and potential in the saturation zone of the form,

$$(E_r, E_\theta) = \left(0, -\frac{1}{r}\frac{\partial F}{\partial \theta}\right), \quad \phi = F(\theta), \tag{B4}$$

where F is a function determined by matching (B4) with the potential of the surrounding singular field (54) on the boundary ($\bar{r} = R$). The potential in the unsaturated region which cooresponds to (54) is

$$\phi = -\sqrt{\frac{h\bar{r}}{\pi}} E_o \cos(\bar{\theta}/2). \tag{B5}$$

On the saturated zone boundary, θ and $\bar{\theta}$ are related by

$$\bar{\theta} = 2\theta - \pi \quad \text{for} \quad \frac{\pi}{2} < \theta < \pi \quad \text{and} \quad \bar{\theta} = 2\theta + \pi \quad \text{for} \quad -\pi < \theta < -\frac{\pi}{2}. \tag{B6}$$

Using (B5–6), the potential on the boundary is

$$\phi = -\sqrt{\frac{hR}{\pi}} E_o \sin\theta \quad \text{for} \quad \frac{\pi}{2} < \theta < \pi \quad \text{and}$$

$$\phi = \sqrt{\frac{hR}{\pi}} E_o \sin\theta \quad \text{for} \quad -\pi < \theta < -\frac{\pi}{2}. \tag{B7}$$

Matching this with (B4) gives

$$\phi = -\sqrt{\frac{hR}{\pi}} E_o \sin\theta, \quad E_\theta = \sqrt{\frac{hR}{\pi}} \frac{E_o}{r} \cos\theta \quad \text{for} \quad \frac{\pi}{2} < \theta < \pi \quad \text{and}$$

$$\phi = \sqrt{\frac{hR}{\pi}} E_o \sin\theta, \quad E_\theta = -\sqrt{\frac{hR}{\pi}} \frac{E_o}{r} \cos\theta \quad \text{for} \quad -\pi < \theta < -\frac{\pi}{2} \tag{B8}$$

in the saturated region. Equation (B8) shows that lines of constant potential are arranged in a fan centered at the electrode tip as shown in Fig. B2. The polarization on the boundary is

$$P_r = 0, \quad P_\theta = -P_s k E_o \sqrt{\frac{h}{\pi R}} \quad \text{for} \quad \frac{\pi}{2} < \theta < \pi \quad \text{and}$$

$$P_r = 0, \quad P_\theta = P_s k E_o \sqrt{\frac{h}{\pi R}} \quad \text{for} \quad -\pi < \theta < -\frac{\pi}{2}. \tag{B9}$$

From (B3) and (B9), continuity of the polarization across the boundary is satisfied if

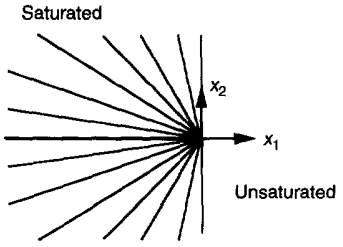

Fig. B3. Approximation of the saturation zone used for the mechanical solution of the internal electrode.

$$P_s = P_s k E_o \sqrt{\frac{h}{\pi R}} \quad \text{or} \quad R = (kE_o)^2 \frac{h}{\pi}. \tag{B10}$$

Directly ahead of the electrode tip ($\theta = 0$) the electric field in the unsaturated region is

$$E_1 = E_o \sqrt{\frac{h}{\pi(r+R)}}. \tag{B11}$$

Now we consider the mechanical portion of the problem. For simplicity, we assume that the region behind the electrode tip ($x_1 < 0$) is completely saturated, while the region ahead of the tip ($x_1 > 0$) is unsaturated as shown in Fig. B3. This approximates the mechanical state in the circular saturation zone near the tip, when R is large. Equilibrium in the actuator is satisfied by the introduction of the Airy stress function Φ. The electrically induced strain in the saturation zone is given by (37) with the polarization field defined by (B3). Following Yang and Suo (1994) we assume that the induced strain outside the saturation zone is zero. So the strains and displacements in terms of polar coordinates are

$$\begin{aligned}
\varepsilon_{rr} &= -\frac{(1+\nu)}{Y}\frac{\partial^2\Phi}{\partial r^2} + \frac{(1-\nu^2)}{Y}\nabla^2\Phi + (1+\nu)Q_{12}P_s^2 \\
\varepsilon_{\theta\theta} &= -\frac{(1+\nu)}{Y}\left(\frac{1}{r}\frac{\partial\Phi}{\partial r} + \frac{1}{r^2}\frac{\partial^2\Phi}{\partial\theta^2}\right) + \frac{(1-\nu^2)}{Y}\nabla^2\Phi + (Q_{11} - \nu Q_{12})P_s^2 \\
\varepsilon_{r\theta} &= -\frac{(1+\nu)}{Y}\frac{\partial}{\partial r}\left[\frac{1}{r}\frac{\partial\Phi}{\partial\theta}\right]
\end{aligned} \tag{B12}$$

$$\begin{aligned}
u_r &= -\frac{(1+\nu)}{Y}\frac{\partial\Phi}{\partial r} + \frac{4(1-\nu^2)}{Y}\,\mathrm{Real}(\Omega\, e^{i\theta}) + (1+\nu)Q_{12}P_s^2 r \\
u_\theta &= -\frac{(1+\nu)}{Yr}\frac{\partial\Phi}{\partial\theta} + \frac{4(1-\nu^2)}{Y}\,\mathrm{Real}(i\Omega\, e^{i\theta}) + (Q_{11} - Q_{12})P_s^2 r\theta.
\end{aligned} \tag{B13}$$

Ω is a complex function of $z = x_1 + ix_2$ defined by

$$\nabla^2\Phi = \sigma_{rr} + \sigma_{\theta\theta} = 4\,\mathrm{Real}\,\Omega(z). \tag{B14}$$

and $i = \sqrt{-1}$. In the unsaturated region, the non-homogenous electrostrictive terms in (B12–13) are zero. Using (B12) it can be shown that compatibility of the total strain is satisfied if

$$\nabla^4\Phi = 0 \tag{B15}$$

in both the saturated and unsaturated regions. The stress function must also fulfill the traction and displacement continuity requirements across the zone boundary ($x_1 = 0$) and the symmetry condition of $u_\theta = 0$ on $x_2 = 0$. These requirements and (B15) are satisfied by the solution,

$$\begin{aligned}
\Phi &= -\frac{(Q_{11} - Q_{12})P_s^2 Y}{8(1-\nu^2)} r^2 \ln r + \Phi_o(r,\theta) \quad \text{for} \quad x_1 < 0 \quad \text{and} \\
\Phi &= -\frac{(Q_{11} - Q_{12})P_s^2 Y}{8(1-\nu^2)} r^2 \ln r + \frac{Q_{12}P_s^2 Y}{2(1-\nu)} r^2 \cos^2\theta + \Phi_o(r,\theta) \quad \text{for} \quad x_1 > 0
\end{aligned} \tag{B16}$$

where Φ_o is the portion of the stress function which contains additional nonsingular stress terms. The singular stresses that result from (B16) are

$$\sigma_{rr} = \sigma_{\theta\theta} = -\frac{(Q_{11}-Q_{12})P_s^2 Y}{4(1-\nu^2)} \ln r, \quad \sigma_{r\theta} = 0. \tag{B17}$$